Geophysical Research Letters

Key Points:
- Poleward Atlantic Water transport is 4.6 ± 0.2 Sv along the Mohn Ridge
- Seasonality in deep currents leads to a maximum transport in the fall
- Volume transport variations were anticorrelated with wind stress curl sign over the Lofoten Basin

Supporting Information:
- Supporting Information S1

Correspondence to:
A. Bosse,
anthony.bosse@uib.no

Mean Structure and Seasonality of the Norwegian Atlantic Front Current Along the Mohn Ridge From Repeated Glider Transects

Anthony Bosse[1] [iD] **and Ilker Fer[1]** [iD]

[1]Geophysical Institute, Bjerknes Center for Climate Research, University of Bergen, Bergen, Norway

Abstract The poleward flow of Atlantic Water in the Nordic Seas forms the upper limb of the meridional overturning circulation driving an important heat transport. The Norwegian Atlantic Front Current along the Mohn Ridge between the Greenland and Norwegian Seas is characterized for the first time, using repeated sections over 14 months from autonomous underwater gliders and two research cruises. The Norwegian Atlantic Front Current follows the 2,550-m isobath with a width of about 60 km and absolute geostrophic velocities peaking at about $0.45\ \mathrm{m\ s^{-1}}$. The mean transport of Atlantic Water is 4.6 ± 0.2 Sv (equivalent to temperature transport of 100 ± 6 TW). Seasonal variability was observed with an amplitude of 0.9 Sv and maximum values in the fall. The deep currents at 1,000 m explained most of this seasonal variation and were anticorrelated with time-integrated wind stress curl over the Lofoten Basin. Part of this flow might recirculate within the Lofoten Basin, while the rest continues toward the Arctic.

1. Introduction

Ocean circulation plays a key role in the climate system by redistributing heat from low to high latitudes (Ganachaud & Wunsch, 2000). The upper limb of the meridional overturning circulation in the Atlantic carries warm and salty Atlantic Water (AW) poleward across the north Atlantic toward the Arctic Ocean. The role of Nordic Seas (Greenland, Iceland, and Norwegian Seas) in the meridional overturning circulation, through heat exchanges with the atmosphere and production of North Atlantic deep water, is increasingly recognized (Chafik & Rossby, 2019; Lozier et al., 2019). The transport of AW affects the climate of western Europe (Årthun et al., 2017; Rhines et al., 2008), water mass transformation (Bosse et al., 2018; Mauritzen, 1996; Rossby et al., 2009), sea ice extent (Lind et al., 2018; Onarheim et al., 2014), as well as marine ecosystems (Årthun et al., 2018; Fossheim et al., 2015; Oziel et al., 2017). Characterizing the structure, magnitude and variability of this poleward transport is therefore highly important.

The ocean currents carrying warm AW in the Nordic Seas are organized in two poleward branches (Orvik & Niiler, 2002) (Figure 1a): the barotropic Norwegian Atlantic Slope Current (NwASC) and the baroclinic Norwegian Atlantic Front Current (NwAFC). The NwASC follows the shelf break northward and continues to the Barents Sea and Fram Strait. The NwAFC is the western branch and follows the 2,000-m isobath along the Vøring Plateau and then the Mohn and the Knipovich ridges farther north (Orvik & Niiler, 2002) (see Figure 1a and supporting information Figure S1 for a detailed bathymetric map of the Mohn Ridge region), before it partly joins the Fram Strait branch and recirculates into the Greenland Sea. Along their poleward pathway, the slope and frontal branches exchange waters (Rossby et al., 2009) and a slab of AW fills the Lofoten Basin (LB), forming the largest heat and salt reservoir of the Nordic Seas (Björk et al., 2001; Bosse et al., 2018; Mork et al., 2014; see Figure S2).

South of the Vøring Plateau at the Svinøy section (63° N), continuous measurements since 1995 set the NwASC annual transport to 4.2–4.4 Sv (Orvik & Skagseth, 2003; Orvik et al., 2001) ($\mathrm{Sv} = 10^6\ \mathrm{m^3\ s^{-1}}$). This barotropic branch is relatively well constrained by observations. Transport of the NwAFC in the same section, on the other hand, is highly uncertain. Based on limited hydrographic data and assuming a deep level of no motion, a baroclinic geostrophic transport estimate was 3.4 Sv (Orvik et al., 2001). Similar baroclinic transport calculations using limited surveys gave 2.4 Sv over the Mohn Ridge (Gascard et al., 2004), 2.6 Sv (Walczowski et al., 2005) and 3 Sv (van Aken et al., 1995) over the Knipovich Ridge. While these transports are roughly consistent, all exclude the barotropic contribution which was suggested to be important using theoretical arguments (Orvik, 2004), limited deep current profiling (Walczowski et al., 2005), and
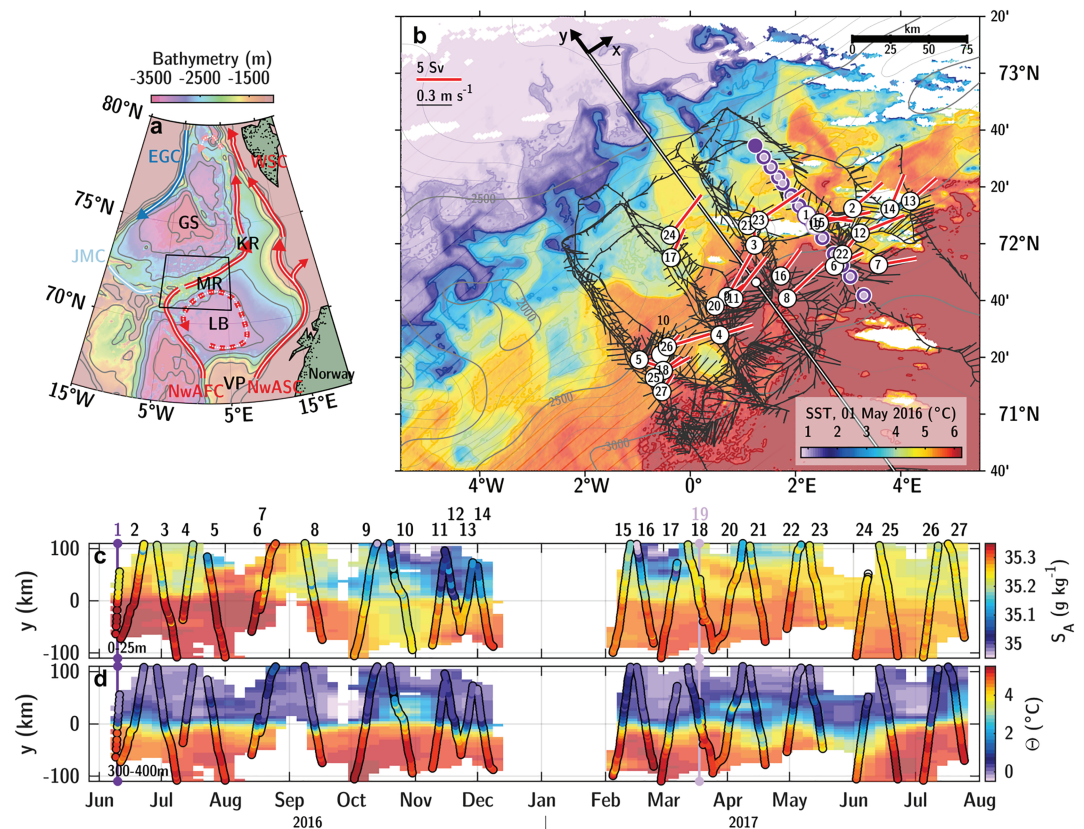
Figure 1. (a) Bathymetric map of the Nordic Seas from global ETOPO gridded data. Bathymetry contours smoothed at 25-km are shown every 500 m (in gray). The main currents and bathymetric features are annotated: Norwegian Atlantic Slope and Front Current (NwASC and NwAFC), West Spitsbergen Current (WSC), East Greenland Current (EGC), Jan Mayen Current (JMC), Mohn Ridge (MR), Knipovitch Ridge (KR), Vøring Plateau (VP), Lofoten Basin (LB), and Greenland Sea (GS). (b) Trajectory of the glider across the Polar Front with depth-averaged current vectors (black) overlain on a sea surface temperature (SST) image captured by satellite on 1 May 2016. Smoothed isobaths are drawn every 100 m (gray). Red vectors show the AW transport for each individual front crossing (numbered circles) from glider and cruises (Sections 1 and 19). Purple dots are CTD/L-ADCP stations taken during two PROVOLO cruises. The mean position and direction of the individual PF samplings define the mean PF axis. Cross-front distance and time distribution of (c) absolute salinity (0–25 m average) and (d) conservative temperature (300–400 m average) for individual dives (circles) and the objectively interpolated fields with correlation scales of 30 days and 30 km.

absolute geostrophic current calculations referenced to shipboard current measurements (Cisewski et al., 2003). Using Seaglider sections in the NwAFC at the Svinøy section, Høydalsvik et al. (2013) obtained absolute geostrophic transport (referenced to glider depth-averaged currents [DAC]) of 6.8 Sv, that is, larger than the transport of NwASC. Currently, the magnitude and structure of the NwAFC transport are thus poorly constrained by observations.

The LB is characterized by intense winter heat losses to the atmosphere (annual average of 80 W m^{-2}) (Isachsen et al., 2007; Richards & Straneo, 2015), a deep cyclonic circulation (Voet et al., 2010) (dashed line in Figure 1a), and winter mixed layer depths exceeding 500 m (Bosse et al., 2018; Latarius & Quadfasel, 2016; Nilsen & Falck, 2006). Consequently, a sharp and dynamic density front is established over the Mohn Ridge that separates the warm AW from cooler and less saline Arctic waters (Mork & Blindheim, 2000). The NwAFC flows as a baroclinic jet associated with this "Polar Front" (PF; also called "Arctic Front"). The frontal system is hypothesized to contribute approximately half of the total northward AW transport (Gascard et al., 2004; Høydalsvik et al., 2013; Orvik et al., 2001; Walczowski et al., 2005) and to mediate exchanges between the Norwegian and Greenland Seas (Segtnan et al., 2011; van Aken et al., 1995; Walczowski, 2013). However, despite its impact on ocean circulation and biology (van Aken et al., 1991), observations at the PF are scant.

Here, we present detailed observations of the PF and NwAFC along the Mohn Ridge using sustained measurements over a period of 14 months. We report the first accurate estimates of absolute AW transport, as well as its components associated with the deep currents at 1,000 m and with the geostrophic shear above this level. The data are collected from two cruises and repeated transects using autonomous underwater gliders. The average structure is well resolved, and the seasonal variability is discussed within the limitation of the data set. The NwAFC at the Mohn Ridge is a key contributor to redistribution of the AW heat toward the Arctic and must be monitored.

2. Data and Methods

2.1. Cruise Data

Measurements were made under the PROVOLO project ("Water mass transformation processes and vortex dynamics in the LB of the Norwegian Sea"). A 150-km section across the Mohn Ridge was repeated during two PROVOLO cruises with *RV Håkon Mosby* in June 2016 (14 stations) and *RV Kristine Bonnevie* in March 2017 (13 stations). Conductivity-Temperature-Depth profiles were acquired using a Sea-Bird Scientific SBE 911plus with pressure, temperature, and salinity data accurate to ±0.5 dbar, ± 0.002 °C, and ±0.003 g kg^{-1}, respectively. Conservative temperature Θ, absolute salinity S_A, and potential density anomaly σ_Θ were calculated using the TEOS-10 Gibbs Seawater Oceanographic toolbox (McDougall & Barker, 2011). Horizontal current profiles were acquired by a pair of 300-kHz lowered acoustic Doppler current profilers (L-ADCP) attached to the rosette, sampling in 8-m vertical cells. The L-ADCP data were processed using the velocity inversion method of Visbeck (2002), implemented in the LDEO software version IX-12 (Thurnherr, 2010), with typical horizontal velocity uncertainty of 2–3 cm s^{-1}. The data set and further details can be found in Fer et al. (2019).

2.2. Seaglider Missions

Autonomous underwater gliders collect data along a sawtooth trajectory between the surface and a typical maximum depth of 1,000 m (Testor et al., 2019). Between two consecutive dives, an estimate of the DAC is obtained by comparing the dead-reckoning position to accurate GPS fixes. Two Seagliders were deployed successively in June 2016 and January 2017 and repeatedly sampled the PF down to 1,000 m for 14 months with a 1.5-month gap in January 2017. In total, 25 sections were occupied from June 2016 to July 2017 along four main lines spread over about 150 km along the ridge's axis (Figure 1b). No difference in the PF structure could be identified along the ridge. Each section took on average 10 days to be completed, while the frontal zone was crossed in about 3 days. The Seagliders were equipped with unpumped SBE-41 C/T sensors. Average horizontal and vertical speeds were 15 km day^{-1} and 8 cm s^{-1}, respectively, giving a typical horizontal separation between profiles of 2.5 km (5 km between DAC estimates) and a vertical resolution of 0.8–1.6 m with the sampling rate of 10–20 s. Salinity was calculated after a thermal lag correction (Garau et al., 2011). Finally, glider temperature and salinity were corrected by an offset against the calibrated cruise Conductivity-Temperature-Depth profiles. The data set and further details can be found in Bosse and Fer (2019).

2.3. Temperature, Salinity, and Velocity Sections

For the 25 glider sections, along-stream absolute geostrophic velocities were computed in a cross-front axis defined by the direction of DAC, following Todd et al. (2016) and assuming DAC is aligned with the baroclinic surface jet. This hypothesis was validated by L-ADCP profiles in summer, while in winter, a cyclonic rotation of currents with increasing depth was noted. This can be due to β-spiral and surface cooling effects (Schott & Stommel, 1978). The traditional calculation of geostrophic velocities perpendicular to the glider track leads to smaller velocity amplitude, larger apparent width, and similar transport (see Figures S3 and S4 and Table S1 for methodological details). Scattered Θ/S_A were then optimally interpolated on a regular grid using a two-dimensional Gaussian correlation function: $cov(X, Z) = e\delta(X, Z) + (1 - e) \exp(-X^2/L_r^2 - Z^2/L_z^2)$ with δ the Dirac function, $e = 0.05$ the relative error, $L_r = 20$ km, typical half-width of the PF, and $L_z = 15$ m, typical vertical scale of the seasonal thermocline. A 20-km scale corresponds to a sampling time scale of about 32 hr, larger than the dominant tidal (about 12 and 24 hr) and inertial (about 13 hr) periods, effectively filtering internal waves (Rudnick & Cole, 2011). Along-stream geostrophic velocities (U_g) were finally obtained by vertically integrating the geostrophic shear and constraining its depth average by the DAC. The PF position ($y = 0$) was defined as the location where 0- to 50-m averaged velocity was maximum.

For each glider section, absolute geostrophic velocities were decomposed into velocities at 1,000 m ($U_g^{1,000}$) and the remainder due to geostrophic shear above this level (U_g^{shear}) (i.e., equivalent to assuming a level of

no motion at 1,000 m). Seasonal composites were then obtained by averaging sections from different months (winter: JFMA, summer: MJJA, and fall: SOND). These 4-month periods correspond to the short period of heat gain from the atmosphere from May to August and the long period of cooling from September to April (Yu et al., 2017). Finally, the mean PF section was calculated as the average of the three seasonal composites. For a consistent and homogeneous data set, shipboard measurements were not included in the composites but were used to describe the PF characteristics (seasonal and annual means summarized in Table S1). The water mass definitions follow the literature (Blindheim, 1990)—note that absolute salinity is larger by about 0.17 g kg^{-1} compared to practical salinity: AW, $S_A > 35.17$ g kg^{-1}; new AW (nAW), $S_A > 35.27$ g kg^{-1} and $\Theta > 6$ °C; modified AW (mAW), $35.28 < S_A < 35.34$ g kg^{-1} and $27.71 < \sigma_\theta < 27.82$ kg m^{-3}; and Arctic Surface Water (ASW), $S_A < 35.12$ g kg^{-1} for $\sigma_\theta < 27.8$ kg m^{-3} and $S_A < 35.07$ g kg^{-1} otherwise. Mixed layer depths are estimated with a threshold on potential density increase of 0.03 kg m^{-3} (de Boyer Montégut et al., 2004).

2.4. Volume and Temperature Transport

Optimally interpolated sections of U_g and Θ were used to estimate the NwAFC volume and temperature transports. Lateral integration limits for each section were obtained by fitting a Gaussian jet ($U_m e^{-0.5x^2/\sigma^2}$ with U_m the maximum velocity and σ the variance of the Gaussian function) to the depth-averaged geostrophic velocit, restricted to the values above half of the maximum value. Integration limits, also defining the width of the PF (L_{int} in Table S1), were then delineated by regions of poleward velocity (i.e., positive) within the maximum interval of $x = \pm 2\sigma$, accounting for about 95% of the total transport of the theoretical jet. This was motivated to exclude spurious transports away from the front axis, captured because of the slow glider speed (about 3 days to cross the PF). Along-stream velocities were then categorized in different water masses and integrated.

For transports from the cruise data, direct measurements by L-ADCP were used, and the jet axis was defined at the location of maximum in 0- to 200-m depth-averaged velocity. Temperature transport across the PF was computed using a reference temperature of −0.1 °C, the mean temperature of the outflow from the Arctic Ocean (Aagaard & Greisman, 1975). Because these estimates are based on single sections and mass is not conserved, they represent temperature transport rather than heat transport.

Error in DAC from gliders can be considered as a random error of 0.02 m s^{-1} (Rudnick et al., 2018). A statistical analysis on 100 members of each cross-front section by adding random noise to DAC, together with the optimal interpolation error, gave a mean statistical error, averaged over the 25 glider sections, of 0.14 and 0.05 Sv for total and AW transports, respectively. Note that the errors in individual transport estimates are small compared to the standard error of the mean arising due to transect-to-transect variability (Table S1). Cross-front sections were considered as independent if separated in space and time by scales larger than typical mesoscale. In the Nordic Seas, the deformation radius is about 10 km (Nurser & Bacon, 2014). Assuming decorrelation scales of 25 km and 5 days, Sections 5/6 and 18/19 were identified as dependent (Figure 1c) and averaged before computing seasonal means.

2.5. Atmospheric Reanalysis

Atmospheric forcing was obtained from ECMWF's ERA-5 reanalysis for the period from June 2016 to July 2017 (Copernicus Climate Change Service, 2017). Hourly 10-m winds at 0.25° resolution were retrieved and averaged into 24-hr intervals. The daily wind stress was then computed as $\tau_\mathbf{w} = \rho_a Cd_a |v_w| \mathbf{v_w}$, where $\mathbf{v_w}$ is the wind, $\rho_a = 1.2$ kg m^{-3} the air density, and $Cd_a = 0.0012$ the surface drag coefficient for moderate winds (Large & Pond, 1981).

3. Results

3.1. Mean Hydrographic and Current Structure

The AW layer extends to a depth of 700 m in the LB and shoals toward the Mohn Ridge (see Figure S2). As captured by the satellite image in May 2016, the surface temperature across the PF decreased from about 6 to 1 °C through a succession of fronts influenced by mesoscale features (Figure 1b), similar to the PF structure described along the Knipovitch Ridge by van Aken et al. (1995). Higher salinities (about 35.3 g kg^{-1}) were observed on the warm side of the front (Figure 1c), with a freshening trend consistent with recent observations (Bosse et al., 2018; Mork et al., 2019). The salinity on the cold side was more variable and reached minimum values from October to March. This relatively fresh water, associated with ASW, can be linked to seasonal advection of ASW from the Greenland shelf by the Jan Mayen Current (Figure S5). At the depth of
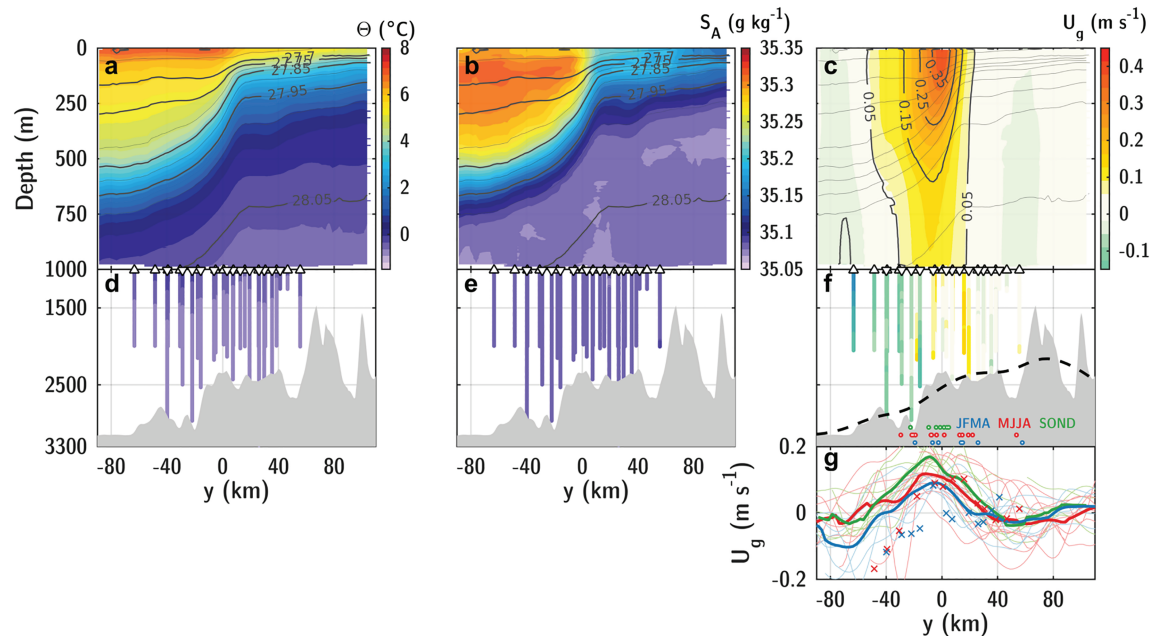
Figure 2. Annual composite of the PF over the Mohn Ridge. Mean section of (a) conservative temperature, (b) absolute salinity, and (c) along-stream geostrophic velocities. The section is seen from the north and positive velocity is directed toward the reader. (d)–(f) are individual CTD/L-ADCP profiles shown only below 1,000 m and collected during the two PROVOLO cruises in June 2016 (upward triangles) and March 2017 (downward triangles). The bathymetry is interpolated on the mean PF section (y axis in Figure 1b) and shown in gray. Dashed black line in (f) represents bathymetry smoothed over a 25-km horizontal scale. Dots show each PF position colored according to seasons. (g) Observed deep velocity field (900–1,000 m average) colored according to seasons. Thin lines show individual glider sections, thick lines are seasonal means, and crosses are shipborne observations by L-ADCP.

the AW core, the PF manifested as an abrupt decrease of temperature of the AW layer (about $-4\,°C/40\,km$ at 300- to 400-m depth; Figure 1d), stronger than at the surface. Instabilities of the front generate important lateral heat fluxes. In particular, warm anticyclonic features detaching from the front could restratify the upper layers on the cold side (Figure 1b).

The composite PF section confirms the existence of a steep temperature front at 200- to 500-m depth and a salinity signature near the surface (Figure 2). The isopycnal slope peaks at the front origin, defining the baroclinic jet of the PF. The geostrophic currents had an average maximum speed of $0.45 \pm 0.02\,m\,s^{-1}$ (mean $\pm$ standard error, standard error $= \sigma/\sqrt{n}$ with σ the standard deviation and n the number of independent cross-front sections) with values ranging from 0.26 to $0.67\,m\,s^{-1}$. The absolute currents at 1,000 m were strong ($0.15 \pm 0.01\,m\,s^{-1}$). The width of the PF was $59 \pm 3\,km$. The PF position over the Mohn Ridge varied by about 100 km across the ridge between the 2,250- and 2,840-m isobaths, with an average at the 2,550-m isobath (with respect to the smoothed topography). This is about half the distance from the bottom to the ridge crest. More variability in PF position was observed during the winter and summer when deep currents were also weaker (Figure 2f). The jet was observed always on the same side of the ridge (i.e., retrograde jet in direction opposite to topographic Rossby waves) indicating stabilization of the barotropic flow (Li & McClimans, 2000; Poulin & Flierl, 2005). The topographic control of the barotropic jet along the Mohn and Knipovitch ridges indicates that parts of the AW could recirculate and flow to the southeast into the LB (Figure S6).

A mean flow in the opposite direction of the poleward frontal current was observed in the LB at about 75 km from the PF. This opposing flow was more intense at depth, with a mean value of about $0.05\,cm\,s^{-1}$, as theoretically predicted by Orvik (2004) and described by Voet et al. (2010) from the drift of Argo floats at middepth. The deep currents directly measured during the cruises confirm the return flow on the warm side of the PF with even larger amplitude (Figure 2f), but they might be influenced by surrounding mesoscale features. The flow associated with the cyclonic circulation was stronger during the winter while almost nil during the summer and fall (Figure 2g), indicating either a decrease in intensity or a shift in position toward the center of the LB.
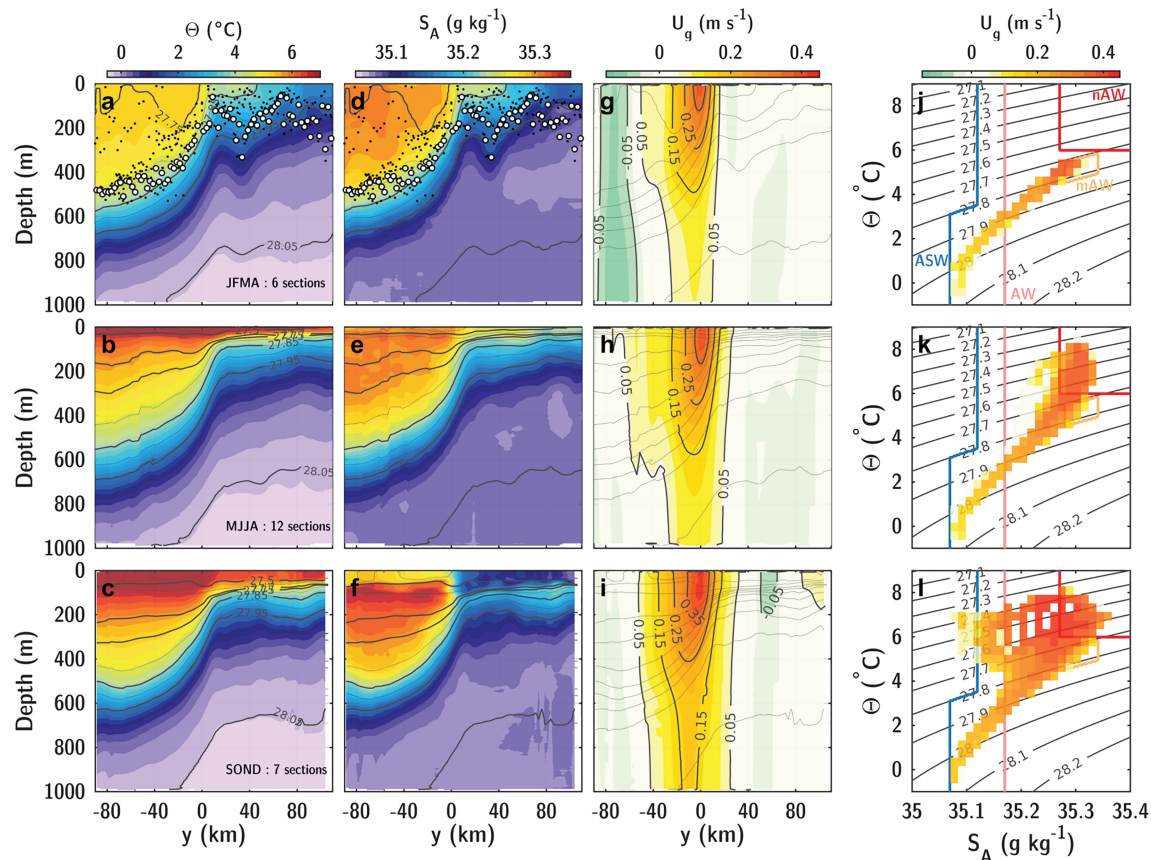
Figure 3. Seasonal evolution of the PF. Vertical section of (a–c) conservative temperature, (d–f) absolute salinity, (g–i) along-stream geostrophic velocities, and (j–l) water mass detection. Dots in (a,d) are MLD estimates (individual observations in black, 75th percentile in white). (j–l) Θ/S_A diagram for each seasonal composite with binned minimum geostrophic velocities of the PF. Line of constant potential density σ_θ are drawn in gray. Areas corresponding to the different water masses are also shown: Atlantic Water (AW), new Atlantic Water (nAW), modified Atlantic Water (mAW), and Arctic Surface Water (ASW).

3.2. Seasonal Evolution

The vertical structure of the PF shows a seasonal evolution (Figure 3). Deep vertical mixing reaching 500 m cooled the AW to form a mode water of about 5.3 °C in winter 2017 (mAW, see Figure 3d). Cross-front exchanges of warm waters prevent deep vertical mixing on the cold side where the mixed layer depth was only about 200 m, in line with the shoaling of the AW pycnocline (i.e., $\sigma_\theta = 27.9\,\mathrm{kg\,m^{-3}}$). This transition zone, characterized in the upper 200 m by an intrusion of relatively cold and fresh AW of about 3 °C, extended to at least 100 km from the PF and was observed in all seasons (Figures 3a–3f), in agreement with climatological observations across the Mohn Ridge (Figure S2). The strongest cross-front temperature and salinity contrasts were detected in the fall. This was due to the presence of a 50-m-thick ASW layer, as well as the arrival of new warm and salty waters (nAW) in summer between 100 and 200 m, originating from the NwASC (Figures 3k and 3l).

Density gradients in the PF were typically dominated by temperature, but salinity gradients reaching $-0.2\,\mathrm{g\,kg^{-1}}$ in fall compensated for approximately one third of the cross-front density increase from temperature. The maximum temperature gradient across the PF increased from winter ($-0.19\,\mathrm{°C\,km^{-1}}$) to fall ($-0.26\,\mathrm{°C\,km^{-1}}$) located at 270- and 210-m depths, respectively. The PF was also broader (68 ± 5 km) with absolute currents at 1,000 m reaching $0.20 \pm 0.02\,\mathrm{m\,s^{-1}}$ in fall, compared to $0.11 \pm 0.02\,\mathrm{m\,s^{-1}}$ in winter and $0.14 \pm 0.01\,\mathrm{m\,s^{-1}}$ in summer. The return flow associated with the deep cyclonic gyre circulation of the LB was captured in winter with a DAC of $0.10\,\mathrm{m\,s^{-1}}$, whereas it was absent in summer and fall.

3.3. Volume and Temperature Transport

The average AW transport was 4.6 ± 0.2 Sv, varying from 2.5 to 6.5 Sv with a seasonal evolution in volume and type of water masses (Figure 4a). The mAW was observed throughout the year but dominated the winter transport with 1.5 ± 0.5 Sv. On the contrary, the nAW was absent during the winter and peaked during the
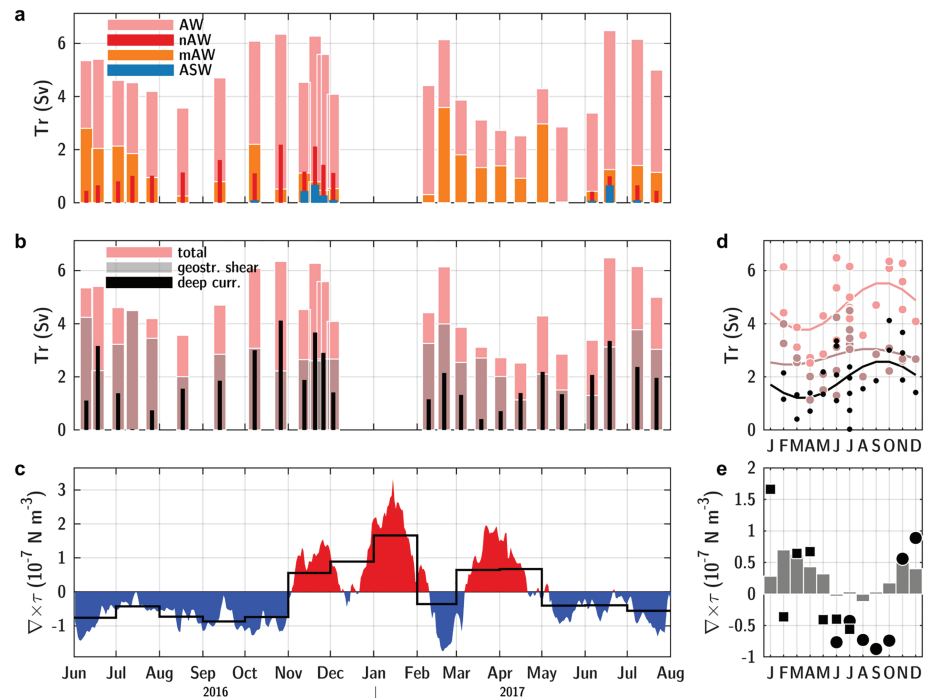
Figure 4. Atlantic Water transport decomposed into (a) different water masses and components associated with (b) geostrophic shear above 1,000 m and deep currents at this depth. (c) Time series of wind stress curl from ERA-5 atmospheric reanalysis (30-day running average computed from daily averaged wind fields and monthly mean in black). Seasonal cycles of (d) the total, geostrophic shear and deep currents AW transports with a sinusoidal fit to the observations and
(e) monthly ERA-5 wind stress curl over the LB (gray bars: 2000–2016 average, circles: 2016, and squares: 2017).

fall (1.5 ± 0.2 Sv). The ASW was occasionally transported with the PF, mostly during the summer and fall: In 7 out of 25 sections, ASW transport was larger than 0.1 Sv, with a maximum of 0.7 Sv observed in November when the surface salinity was the lowest. Note, however, the 2-month gap in the data due to the turnover of the gliders in January.

The AW transport was decomposed into a component associated with the deep currents measured at 1,000 m and the remainder associated with the geostrophic shear above this depth. While the total transport had a marked seasonal signature varying from 3.8 ± 0.6 Sv in winter to 5.4 ± 0.3 Sv in the fall, the transport due to geostrophic shear was fairly constant with 2.7 ± 0.2 Sv. This transport is in good agreement with previous estimates along the Mohn Ridge (Gascard et al., 2004; Orvik, 2004) and farther north (van Aken et al., 1995; Walczowski et al., 2005). The seasonal variation in AW transport was thus primarily due to variation in the transport associated with deep currents that doubled from the winter (1.2 ± 0.2 Sv, 26% of the total AW transport) to the fall (2.7 ± 0.4 Sv, 59% of the total AW transport). Sinusoidal fits to the observed seasonal transport yielded minimum transport in March and amplitudes of 0.3, 0.7, and 0.9 Sv for the geostrophic shear, deep currents, and total transports, respectively (Figure 4c). We conclude that the AW transport at the PF is dominated by currents associated with the geostrophic shear above 1,000 m with a seasonal variability due to deep currents, representative of the barotropic circulation.

The poleward temperature transport at the PF was 100 ± 6 TW (TW = 10^{12} W). As a comparison, the AW temperature transport (using the same temperature reference) is about 300 TW at the AW inflow into the Nordic Seas (Hansen & Østerhus, 2007) and 30–60 TW toward the Arctic Ocean in Fram Strait (Schauer et al., 2004; Tsubouchi et al., 2018).

The wind stress curl drives variations of the barotropic circulation (e.g., see Voet et al., 2010, for the LB). We averaged the wind stress curl over the central LB, inside the 2,800-m isobath guiding the cyclonic gyre circulation of the LB. On seasonal time scales, low-pressure systems traveling across the Nordic Seas typically result in positive wind stress curl during the winter. In summer, cyclonic activity ceases, and wind stress curl relaxes to negative or small values (Figure 4d). Interestingly, an anticorrelation can be noticed between

the sign of wind stress curl and the AW transport variations. Positive wind stress curl indeed increases the cyclonic LB gyre circulation, although Voet et al. (2010) showed that winds cannot alone explain the gyre variability. Consequently, a decrease in the poleward transport at the PF resulted from a reduction of the barotropic component (induced by a strengthened opposing barotropic circulation).

4. Discussion and Concluding Remarks

Average poleward volume and temperature transports of AW along the Mohn Ridge are 4.6 ± 0.2 Sv and 100 ± 6 TW. The transport associated with deep currents at 1,000 m accounts for about 40% of the total. This transport component, documented for the first time here, has often been neglected in previous studies mainly due to limitation of hydrographic surveys without direct currents measurements. The NwAFC is at least as strong as the slope current at the Svinøy section (63° N). Contrary to costly regular ship surveys, the glider technology can be effectively used to monitor topographically steered frontal currents such as the NwAFC. In particular, the fate of the flow of AW downstream of the Mohn Ridge remains unclear. Its connection with the Knipovitch Ridge and farther north to Fram Strait could be investigated by sustained sampling using autonomous underwater gliders.

We found an anticorrelation between the AW transport variations along the Mohn Ridge and the sign of the wind stress curl over the LB. Previous studies have established a positive correlation between the AW transport along the Svinøy slope and the local wind forcing and the large-scale North Atlantic Oscillation (Orvik & Skagseth, 2003a; Skagseth, 2004; Skagseth et al., 2004). The NwAFC and NwASC seem to react in opposite ways to the wind forcing in the LB. Numerical models could help understand the response of the slope and frontal Norwegian Atlantic Currents in the LB where observationsremain scarce.

Deep velocities of 0.1–0.2 cm s^{-1} have been directly measured by lowered profilers. The large abyssal velocities should have important implications for mixing over the rough topography of the Mohn Ridge (Figure S1). The interaction of the barotropic jet of the PF and tides with numerous seamounts of $O(1$–10 km) horizontal scales found along the ridge could generate internal waves and turbulent mixing (Nikurashin & Ferrari, 2011). Moreover, the Mohn Ridge is an active hydrothermal vent (Schander et al., 2010), for which small-scale currents and mixing are important (Vic et al., 2018). The mixing generated by the barotropic component of the frontal current and tides is still unknown and needs further investigations.

The PF position over the ridge slope was fairly stable in the fall, when the frontal jet was more intense and characterized by stronger deep currents. The horizontal shear of deep currents, however, remained quite comparable throughout the year. Topograpic slope plays an important role in the development of barotropic and baroclinic instabilities (Isachsen, 2015; Li & McClimans, 2000). The PF had shallower water on its cyclonic flank (i.e., in the opposite direction of topographic Rossby wave propagation), which is known to stabilize the flow (Poulin & Flierl, 2005). Variable winds associated with low-pressure systems can also excite upstream-propagating topographic Rossby waves (Li & McClimans, 1998). The strong variability in temperature and salinity across the PF captured by Seagliders and a satellite image suggest that the PF instability can be important and deserves further studies. A thorough understanding of the cross-front exchanges is indeed required to assess the role of lateral fluxes in setting the water column stratification and the local ecosystem dynamics, as well as in the propagation of heat and salt anomalies toward the Greenland Sea.

References

Aagaard, K., & Greisman, P. (1975). Toward new mass and heat budgets for the Arctic Ocean. *Journal of Geophysical Research*, *80*(27), 3821–3827. Retrieved from https://doi.org/10.1029/JC080i027p03821

Årthun, M., Bogstad, B., Daewel, U., Keenlyside, N. S., Sandø, A. B., Schrum, C., & Ottersen, G. (2018). Climate based multi-year predictions of the Barents Sea cod stock. *PLOS ONE*, *13*(10), 1–13. https://doi.org/10.1371/journal.pone.0206319

Årthun, M., Eldevik, T., Viste, E., Drange, H., Furevik, T., Johnson, H. L., & Keenlyside, N. S. (2017). Skillful prediction of northern climate provided by the ocean. *Nature Communications*, *8*, 15875. https://doi.org/10.1038/ncomms15875

Björk, G., Gustafsson, B. G., & Stigebrandt, A. (2001). Upper layer circulation of the Nordic seas as inferred from the spatial distribution of heat and freshwater content and potential energy. *Polar Research*, *20*(2), 161–168. https://doi.org/10.1111/j.1751-8369.2001.tb00052.x

Blindheim, J. (1990). Arctic intermediate water in the Norwegian Sea. *Deep Sea Research Part A. Oceanographic Research Papers*, *37*(9), 1475–1489. https://doi.org/10.1016/0198-0149(90)90138-L

Bosse, A., & Fer, I. (2019). Seaglider missions in the Norwegian Sea during the PROVOLO project. https://doi.org/10.21335/NMDC-980686647

Bosse, A., Fer, I., Søiland, H., & Rossby, T. (2018). Atlantic Water transformation along its poleward pathway across the Nordic Seas. *Journal of Geophysical Research: Oceans*, *123*, 6428–6448. https://doi.org/10.1029/2018JC014147

Chafik, L., & Rossby, T. (2019). Volume, heat, and freshwater divergences in the subpolar North Atlantic suggest the Nordic Seas as key to the state of the meridional overturning circulation. *Geophysical Research Letters*, *46*, 4799–4808. https://doi.org/10.1029/2019GL082110

Cisewski, B., Budéus, G., & Krause, G. (2003). Absolute transport estimates of total and individual water masses in the northern Greenland Sea derived from hydrographic and acoustic Doppler current profiler measurements. *Journal of Geophysical Research*, *108*(C9), 3298. https://doi.org/10.1029/2002JC001530

Copernicus Climate Change Service (2017). ERA5: Fifth generation of ECMWF atmospheric reanalyses of the global climate. Retrieved from https://cds.climate.copernicus.eu/cdsapp#!/home

de Boyer Montégut, C., Madec, G., Fischer, A. S., Lazar, A., & Iudicone, D. (2004). Mixed layer depth over the global ocean: An examination of profile data and a profile-based climatology. *Journal of Geophysical Research*, *109*, C12003. https://doi.org/10.1029/2004JC002378

Fer, I., Bosse, A., Søiland, H., Ferron, B., & Bouruet-Aubertot, P. (2019). Ocean currents, hydrography and microstructure data from PROVOLO cruises. https://doi.org/10.21335/NMDC-1093031037

Fossheim, M., Primicerio, R., Johannesen, E., Ingvaldsen, R. B., Aschan, M. M., & Dolgov, A. V. (2015). Recent warming leads to a rapid borealization of fish communities in the Arctic. *Nature Climate Change*, *5*(7), 673–677. https://doi.org/10.1038/nclimate2647

Ganachaud, A., & Wunsch, C. (2000). Oceanic meridional overturning circulation, mixing, bottom water formation rates and heat transport. *Nature*, *408*, 453–456.

Garau, B., Ruiz, S., Zhang, W. G., Pascual, A., Heslop, E. E., Kerfoot, J., & Tintoré, J. (2011). Thermal lag correction on Slocum CTD glider data. *Journal of Atmospheric and Oceanic Technology*, *28*(9), 1065–1071. https://doi.org/10.1175/JTECH-D-10-05030.1

Gascard, J.-C., Raisbeck, G., Sequeira, S., Yiou, F., & Mork, K. A. (2004). The Norwegian Atlantic Current in the Lofoten basin inferred from hydrological and tracer data (^{129}I) and its interaction with the Norwegian Coastal Current. *Geophysical Research Letters*, *31*, L01308. https://doi.org/10.1029/2003GL018303

Hansen, B., & Østerhus, S. (2007). Faroe Bank Channel overflow 1995–2005. *Progress in Oceanography*, *75*(4), 817–856. https://doi.org/10.1016/j.pocean.2007.09.004

Høydalsvik, F., Mauritzen, C., Orvik, K. A., LaCasce, J. H., Lee, C. M., & Gobat, J. (2013). Transport estimates of the Western Branch of the Norwegian Atlantic Current from glider surveys. *Deep-Sea Research Part I*, *79*(0), 86–95. https://doi.org/10.1016/j.dsr.2013.05.005

Isachsen, P. E. (2015). Baroclinic instability and the mesoscale eddy field around the Lofoten Basin. *Journal of Geophysical Research: Ocean*, *120*, 2884–2903. https://doi.org/10.1002/2014JC010448

Isachsen, P. E., Mauritzen, C., & Svendsen, H. (2007). Dense water formation in the Nordic Seas diagnosed from sea surface buoyancy fluxes. *Deep Sea Research Part I: Oceanographic Research Papers*, *54*(1), 22–41. https://doi.org/10.1016/j.dsr.2006.09.008

Large, W. G., & Pond, S. (1981). Open ocean momentum flux measurements in moderate to strong winds. *Journal of Physical Oceanography*, *11*(3), 324–336. https://doi.org/10.1175/1520-0485(1981)011<0324:OOMFMI>2.0.CO;2

Latarius, K., & Quadfasel, D. (2016). Water mass transformation in the deep basins of the Nordic Seas: Analyses of heat and freshwater budgets. *Deep Sea Research Part I: Oceanographic Research Papers*, *114*, 23–42. https://doi.org/10.1016/j.dsr.2016.04.012

Li, S., & McClimans, T. A. (1998). The effects of winds over a barotropic retrograde slope current. *Continental Shelf Research*, *18*(5), 457–485. https://doi.org/10.1016/S0278-4343(97)00077-0

Li, S., & McClimans, T. A. (2000). On the stability of barotropic prograde and retrograde jets along a bottom slope. *Journal of Geophysical Research*, *105*(C4), 8847–8855. https://doi.org/10.1029/1999JC000006

Lind, S., Ingvaldsen, R. B., & Furevik, T. (2018). Arctic warming hotspot in the northern Barents Sea linked to declining sea-ice import. *Nature Climate Change*, *8*, 634–639. https://doi.org/10.1038/s41558-018-0205-y

Lozier, M. S., Li, F., Bacon, S., Bahr, F., Bower, A. S., Cunningham, S. A., et al. (2019). A sea change in our view of overturning in the subpolar North Atlantic. *Science*, *363*(6426), 516–521. https://doi.org/10.1126/science.aau6592

Mauritzen, C. (1996). Production of dense overflow waters feeding the North Atlantic across the Greenland-Scotland Ridge. 1. Evidence for a revised circulation scheme. *Deep-Sea Research Part I*, *43*, 769–806.

McDougall, T. J., & Barker, P. M. (2011). Getting started with TEOS-10 and the Gibbs Seawater (GSW) Oceanographic Toolbox. SCOR/IAPSO WG127, 28p.

Mork, K. A., & Blindheim, J. (2000). Variations in the Atlantic inflow to the Nordic Seas, 1955–1996. *Deep Sea Research Part I: Oceanographic Research Papers*, *47*(6), 1035–1057. https://doi.org/10.1016/S0967-0637(99)00091-6

Mork, K. A., Skagseth, Ø., Ivshin, V., Ozhigin, V., Hughes, S. L., & Valdimarsson, H. (2014). Advective and atmospheric forced changes in heat and fresh water content in the Norwegian Sea, 1951–2010. *Geophysical Research Letters*, *41*, 6221–6228. https://doi.org/10.1002/2014GL061038

Mork, K. A., Skagseth, Ø., & Søiland, H. (2019). Recent warming and freshening of the Norwegian Sea observed by Argo data. *Journal of Climate*, *32*(12), 3695–3705. https://doi.org/10.1175/JCLI-D-18-0591.1

Nikurashin, M., & Ferrari, R. (2011). Global energy conversion rate from geostrophic flows into internal lee waves in the deep ocean. *Geophysical Research Letters*, *38*, L08610. https://doi.org/10.1029/2011GL046576

Nilsen, J. E. Ø., & Falck, E. (2006). Variations of mixed layer properties in the Norwegian Sea for the period 1948–1999. *Progress in Oceanography*, *70*(1), 58–90. https://doi.org/10.1016/j.pocean.2006.03.014

Nurser, A. J. G., & Bacon, S. (2014). The Rossby radius in the Arctic Ocean. *Ocean Science*, *10*(6), 967–975. https://doi.org/10.5194/os-10-967-2014

Onarheim, I. H., Smedsrud, L. H., Ingvaldsen, R. B., & Nilsen, F. (2014). Loss of sea ice during winter north of Svalbard. *Tellus A: Dynamic Meteorology and Oceanography*, *66*(1), 23933. https://doi.org/10.3402/tellusa.v66.23933

Orvik, K. A. (2004). The deepening of the Atlantic water in the Lofoten Basin of the Norwegian Sea, demonstrated by using an active reduced gravity model. *Geophysical Research Letters*, *31*, L01306. https://doi.org/10.1029/2003GL018687

Orvik, K. A., & Niiler, P. (2002). Major pathways of Atlantic water in the northern North Atlantic and Nordic Seas toward Arctic. *Geophysical Research Letters*, *29*(19), 1896. https://doi.org/10.1029/2002GL015002

Orvik, K. A., & Skagseth, Ø. (2003). Monitoring the Norwegian Atlantic slope current using a single moored current meter. *Continental Shelf Research*, *23*(2), 159–176. https://doi.org/10.1016/S0278-4343(02)00172-3

Orvik, K. A., & Skagseth, S. (2003a). The impact of the wind stress curl in the North Atlantic on the Atlantic inflow to the Norwegian Sea toward the Arctic. *Geophysical Research Letters*, *30*(17), 1884. https://doi.org/10.1029/2003GL017932

Orvik, K. A., Skagseth, Ø., & Mork, M. (2001). Atlantic inflow to the Nordic Seas: Current structure and volume fluxes from moored current meters, VM-ADCP and SeaSoar-CTD observations, 1995-1999. *Deep Sea Research Part I: Oceanographic Research Papers*, *48*(4), 937–957. https://doi.org/10.1016/S0967-0637(00)00038-8

Oziel, L., Neukermans, G., Ardyna, M., Lancelot, C., Tison, J.-L., Wassmann, P., et al. (2017). Role for Atlantic inflows and sea ice loss on shifting phytoplankton blooms in the Barents Sea. *Journal of Geophysical Research: Oceans*, *122*, 5121–5139. https://doi.org/10.1002/2016JC012582

Poulin, F. J., & Flierl, G. R. (2005). The influence of topography on the stability of jets. *Journal of Physical Oceanography*, *35*(5), 811–825. https://doi.org/10.1175/JPO2719.1

Rhines, P., Häkkinen, S., & Josey, S. A. (2008). Is oceanic heat transport significant in the climate system? In R. R. Dickson, J. Meincke, & P. Rhines (Eds.), *Arctic–Subarctic ocean fluxes: Defining the role of the northern seas in climate* (pp. 87–109). Dordrecht, Netherlands: Springer.

Richards, C. G., & Straneo, F. (2015). Observations of water mass transformation and eddies in the Lofoten Basin of the Nordic Seas. *Journal of Physical Oceanography*, *45*(6), 1735–1756. https://doi.org/10.1175/JPO-D-14-0238.1

Rossby, T., Prater, M. D., & Søiland, H. (2009). Pathways of inflow and dispersion of warm waters in the Nordic Seas. *Journal of Geophysical Research*, *114*, C04011. https://doi.org/10.1029/2008JC005073

Rudnick, D. L., & Cole, S. T. (2011). On sampling the ocean using underwater gliders. *Journal of Geophysical Research*, *116*, C08010. https://doi.org/10.1029/2010JC006849

Rudnick, D. L., Sherman, J. T., & Wu, A. P. (2018). Depth-average velocity from spray underwater gliders. *Journal of Atmospheric and Oceanic Technology*, *35*(2011), 1665–1673. https://doi.org/10.1175/JTECH-D-17-0200.1

Schander, C., Rapp, H. T., Kongsrud, J. A., Bakken, T., Berge, J., Cochrane, S., et al. (2010). The fauna of hydrothermal vents on the Mohn Ridge (north Atlantic). *Marine Biology Research*, *6*(2), 155–171. https://doi.org/10.1080/17451000903147450

Schauer, U., Fahrbach, E., Østerhus, S., & Rohardt, G. (2004). Arctic warming through the Fram Strait: Oceanic heat transport from 3 years of measurements. *Journal of Geophysical Research*, *109*, C06026. https://doi.org/10.1029/2003JC001823

Schott, F., & Stommel, H. (1978). Beta spirals and absolute velocities in different oceans. *Deep-Sea Research*, *25*, 961–1010.

Segtnan, O. H., Furevik, T., & Jenkins, A. D. (2011). Heat and freshwater budgets of the Nordic Seas computed from atmospheric reanalysis and ocean observations. *Journal of Geophysical Research*, *116*, C11003. https://doi.org/10.1029/2011JC006939

Skagseth, Ø. (2004). Monthly to annual variability of the Norwegian Atlantic slope current: Connection between the northern North Atlantic and the Norwegian Sea. *Deep Sea Research Part I: Oceanographic Research Papers*, *51*(3), 349–366. https://doi.org/10.1016/j.dsr.2003.10.014

Skagseth, Ø., Orvik, K. A., & Furevik, T. (2004). Coherent variability of the Norwegian Atlantic slope current derived from TOPEX/ERS altimeter data. *Geophysical Research Letters*, *31*, L14304. https://doi.org/10.1029/2004GL020057

Testor, P., de Young, B., Rudnick, D., Glenn, S., Hayes, D., Lee, C. M., et al. (2019). OceanGliders: A component of the integrated GOOS. *Frontiers in Marine Science*, *6*, 422. https://doi.org/10.3389/fmars.2019.00422

Thurnherr, A. M. (2010). A practical assessment of the errors associated with full-depth LADCP profiles obtained using Teledyne RDI Workhorse acoustic Doppler current profilers. *Journal of Atmospheric and Oceanic Technology*, *27*(7), 1215–1227. https://doi.org/10.1175/2010JTECHO708.1

Todd, R. E., Owens, W. B., & Rudnick, D. L. (2016). Potential vorticity structure in the North Atlantic western boundary current from underwater glider observations. *Journal of Physical Oceanography*, *46*(1), 327–348. https://doi.org/10.1175/JPO-D-15-0112.1

Tsubouchi, T., Bacon, S., Aksenov, Y., Naveira Garabato, A. C., Beszczynska-Möller, A., Hansen, E., et al. (2018). The Arctic ocean seasonal cycles of heat and freshwater fluxes: Observation-based inverse estimates. *Journal of Physical Oceanography*, *48*(9), 2029–2055. https://doi.org/10.1175/JPO-D-17-0239.1

van Aken, H. M., Budéus, G., & Hähnel, M. (1995). The anatomy of the Arctic frontal zone in the Greenland Sea. *Journal of Geophysical Research*, *100*(C8), 15,999–16,014. https://doi.org/10.1029/95JC01176

van Aken, H. M., Quadfasel, D., & Warpakowski, A. (1991). The Arctic front in the Greenland Sea during February 1989: Hydrographic and biological observations. *Journal of Geophysical Research*, *96*(C3), 4739–4750. https://doi.org/10.1029/90JC02271

Vic, C., Gula, J., Roullet, G., & Pradillon, F. (2018). Dispersion of deep-sea hydrothermal vent effluents and larvae by submesoscale and tidal currents. *Deep Sea Research Part I: Oceanographic Research Papers*, *133*, 1–18. https://doi.org/10.1016/j.dsr.2018.01.001

Visbeck, M. (2002). Deep velocity profiling using lowered acoustic Doppler current profilers: Bottom track and inverse solutions. *Journal of Atmospheric and Oceanic Technology*, *19*(5), 794–807.

Voet, G., Quadfasel, D., Mork, K. A., & Søiland, H. (2010). The mid-depth circulation of the Nordic Seas derived from profiling float observations. *Tellus A*, *62*(4), 516–529. https://doi.org/10.1111/j.1600-0870.2010.00444.x

Walczowski, W. (2013). Frontal structures in the West Spitsbergen Current margins. *Ocean Science*, *9*(6), 957–975. https://doi.org/10.5194/os-9-957-2013

Walczowski, W., Piechura, J., Osinski, R., & Wieczorek, P. (2005). The West Spitsbergen Current volume and heat transport from synoptic observations in summer. *Deep-Sea Research Part I*, *52*, 1374–1391.

Yu, L.-S., Bosse, A., Fer, I., Orvik, K. A., Bruvik, E. M., Hessevik, I., & Kvalsund, K. (2017). The Lofoten Basin eddy: Three years of evolution as observed by Seagliders. *Journal of Geophysical Research: Oceans*, *122*, 6814–6834. https://doi.org/10.1002/2017JC012982